NUMERICAL ANALYSIS OF SECONDARY FLOW TOPOLOGIES OF LOW-SPEED AXIAL FANS FROM COMPRESSOR TO LOAD-CONTROLLED WINDMILL

S-K. Courty-Audren - A. Ortolan*† - X. Carbonneau* - N. Binder* - F. Challas†*

* Université de Toulouse, ISAE-SUPAERO
10 avenue Edouard Belin 31400 Toulouse, France
aurelie.ortolan@isae.fr - suk-kee.courty-audren@isae.fr - xavier.carbonneau@isae.fr - nicolas.binder@isae.fr

† SAFRAN Technofan
10 place Marcel Dassault 31700 Blagnac, France
aurelie.ortolan@isae.fr - florent.challas@technofan.com

ABSTRACT

This paper presents the detailed analysis of the local topology evolution from compressor mode to loaded windmill. A first objective is to identify generic patterns of rotor separation topology at windmill and bring light on the mechanisms responsible for it. This study also aims at numerically providing new elements of understanding on tip leakage flows and curvature effects while shifting from compressor to turbine operation. Two machines were investigated : a conventional fan and an innovative design meant to reach both high compressor and turbine efficiencies. In compressor or turbine operation, the tip leakage flow is located on the blade suction side. However, the location of the latter is inverted from one mode to the other. The inversion of the pressure gradient leads, near the hub boundary layer of a blade passage, to an inversion of the cross-flow direction.

KEYWORDS

Windmilling, energy recovery, secondary flows, tip leakage flow, loss mechanisms.

NOMENCLATURE

Supercript

$\bar{\cdot}$	Averaged quantity
$\cdot^*$	Normalized quantity
$\hat{\cdot}$	Assessed at the mean quadratic radius

Subscript

$\cdot_1$	Inlet
$\cdot_2$	Rotor inlet
$\cdot_3$	Rotor Outlet
$\cdot_9$	Outlet
$\cdot_x$	Axial direction

Roman symbols

C_P	Pressure coefficient
n	Normal direction
P_s	Static pressure
P_t	Total pressure
r	Radius (m)
$R_.$	Streamline curvature radius (m)
S	Entropy (J.kg^{-1}K^{-1})
$U = \omega r$	Blade speed (m.s^{-1})
V	Absolute velocity (m.s^{-1})
V_r	Radial absolute velocity (m.s^{-1})
W	Relative velocity (m.s^{-1})

Greek letters

α	Absolute flow angle (°)
$\phi = \frac{V_{x2}}{U}$	Flow coefficient
ϕ_{P}	Flow coefficient at freewindmill
ϕ^*	Reduced flow coefficient
$\psi = \frac{\Delta h_{i23}}{\hat{U}^2}$	Loading coefficient
ω	Angular blade speed (rad.s^{-1})

Abbreviations

Comp.	Absolute flow angle (°)
FW, Free	Freewheeling
LW	Loaded windmill
PS	Pressure side
SS	Suction side

INTRODUCTION

In the aeronautical context, recent studies dealing with windmilling operation are mainly carried out on turbofans in situation of engine flame-out in order to assess restarting and controllability capabilities (Prasad and Lord, 2010; Dufour et al., 2015b). As a consequence, they focus on the freewheeling mode characterized by negligible resistive torque. Another context of windmilling studies is the onboard electrical power generation which aims at providing new energy sources for the so-called more electrical aircrafts. On current aircraft, some machines dedicated to the cooling of onboard heat exchangers are only used during parking, taxiing, and take-off. Those fans are consequently dead weight during cruise and landing. The prospect of turning such devices into electrical generators relies on a strong improvement of the turbine efficiency of compressor systems. In that case, both application and operating range differ from freewheeling situations. Such projects involve load-controlled windmilling operation of low-dimension axial fans (Binder et al., 2015; Ortolan et al., 2016). This mode, also called turbine mode, is located between the freewheeling condition and the locked rotor configuration. Literature (Turner and Sparkes, 1963; Courty-Audren, 2015) reports that classical fan designs are generally characterized by very poor load-controlled windmilling efficiency (around 0.2), due to massive flow separations on the pressure side of the blades (Courty-Audren et al., 2013; Ortolan et al., 2015). However, fans specifically designed for dual functioning present promising turbine and compressor efficiencies (around 0.75 in both modes) as it was numerically assessed in previous works (Ortolan et al., 2015; 2016).

The present paper is interested in identifying generic mechanisms responsible for poor turbine performances of windmilling fans and in emphasizing the resulting generic consequences for designers. On the rotor at windmill, a generic separation shape arises from (Ortolan et al., 2015; Courty-Audren, 2015; Dufour et al., 2015b; Gunn and Hall, 2015), underlined by viscous stress lines on the pressure side. In the present study, the origin of this particular topology is related to endwalls secondary flows and solidity evolution.

Regarding secondary flows, from compressor to turbine modes, the location of pressure and suction sides are inverted. Theoretically, the tangential pressure gradient is responsible for a greater inflexion of the streamline curvature towards the suction side in the endwall regions (Lakshminarayana, 1996; Japikse and Baines, 1997). Consequently, it is expected that from compressor to turbine modes, the streamline curvature is also inverted. As for the tip leakage flow, it comes from pressure differences between the two sides of the blade (Cumpsty, 2004). Consequentely, the location of the tip leakage flow changes from compressor to turbine modes (Courty-Audren, 2015).

The scope of the present study is to analyze the secondary flows local topology of two machines : a conventional fan and a dual functioning fan. The main topics investigated in this paper are the following ones:

- numerical results are confronted to experimental data for the conventional fan and the

optimized design on a local point of view;
- tip leakage flows and curvature effects from compressor to turbine modes are studied based on numerical results for the conventional fan and the optimized design.

PRESENTATION OF THE MACHINES

The machines investigated are low-speed low-dimension axial fans of rotor-stator type: a conventional fan (Fan 1) and one optimized design (Fan 2). The original onboard machine was classically designed as a compressor whereas the optimized fan was designed with a specific procedure allowing high compressor and turbine efficiencies. In these conditions, the compressor design point is not the adequate reference for a comparison. Binder et al. (2015) showed that the reduced flow coefficient, $\hat{\phi}^*$ defined Eq. 1, is the most relevant parameter to compare different machines at the same incursion level in both compressor and turbine modes. Consequently, global and local performances of Fan 1 and Fan 2 are compared for the same reduced flow coefficient values. Experimental values of flow coefficient at freewindmill, $\hat{\phi}_{\mathrm{P}}$, for Fan 1 and Fan 2 are respectively 1.08 and 0.510. The size of the onboard channel imposes the fans diameter to be identical. Thus, the difference in $\hat{\phi}_{\mathrm{P}}$ illustrates that Fan 2 requires higher rotational speeds to reach the same compressor performance. Little information about Fan 2 geometry can be given in this paper since it is confidential. Hatted variables are expressed with the mean quadratic radius:

$$\hat{r} = \sqrt{\frac{r_{shroud}^2 + r_{hub}^2}{2}} \quad ; \quad \hat{\phi}^* = \frac{\hat{\phi}}{\hat{\phi}_{\mathrm{P}}} \tag{1}$$

According to the definition of the reduced flow coefficient (Eq. 1), freewindmill (zero global work) is reached when $\hat{\phi}^* = 1$. Compressor and turbine modes respectively correspond to a value below and above unity. For both machines, local topology was investigated from compressor to turbine mode on the three following operating points: $\hat{\phi}^* = 0.6$, $\hat{\phi}^* = 1$ and $\hat{\phi}^* = 2$. When considering load-controlled widmilling, incidences become even more negative than those reported in freewheeling mode. This can be easily understood thanks to the velocity triangles given on Fig. 1 for compressor, freewheeling and load-controlled windmill modes.

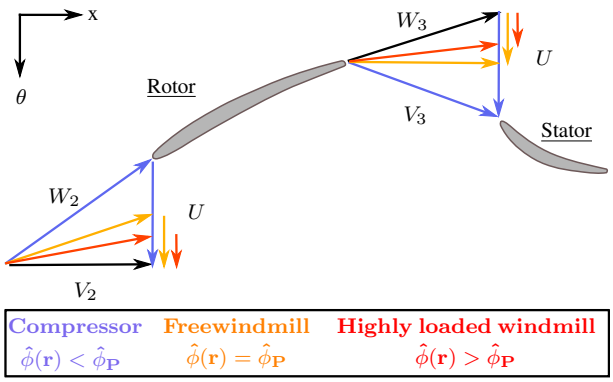

Figure 1: Velocity diagrams from compressor to turbine modes.

EXPERIMENTAL SET UP

A test rig meant for the study of compressor and windmilling operations of low-speed low-dimension axial fans (diameter $\leq$ 200mm) has been implemented in the Department of Aerodynamics, Energetics and Propulsion (DAEP) of ISAE-SUPAERO (Fig. 2). This facility is equipped with an air vacuum system and an asynchronous electrical engine that enable the independent setting of flow generation and shaft loading. This unusual test bed configuration allows to reach every possible operating point from surge limit to locked rotor by regulating the torque applied on the shaft. The instrumented part can be inverted if necessary to change the flow direction. This facility can operate up to Reynolds number of $Re = 200\ 000$ (based on chord) and inlet Mach number of $M_\infty \approx 0.3$.

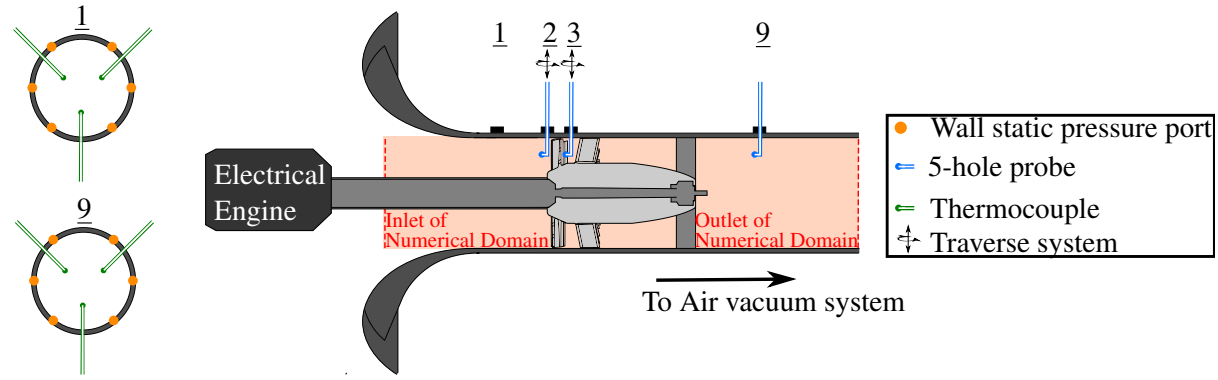

Figure 2: The DAEP test facility and the numerical domain used in this study (orange).

Regarding the instrumentation, for the time being, only steady measurements are conducted. Both global and local ones were implemented to quantify the power recovery and to analyze the flow topology around the rotor (sections 2 and 3). A detailed description of the instrumentation is given in (Ortolan et al., 2016). Uncertainties are calculated from the sensors properties, except the absolute and relative flow angles for which the standard deviation is higher. All the experimental results presented in this study are standardized to suppress the influence of atmospheric pressure and temperature variations during experimental campaigns.

NUMERICAL SET UP

The numerical domain used for the calculations is illustrated in Fig. 2. Contrary to experimental facility, it is not equipped with the bell mouth, shaft and rear support. The overall mesh size is about 2M pts for all machines. The first cell at the wall was set to 4 μm. The mean value of the y^+ parameter at walls is about 0.25 ($y^+_{max} \approx 2.5$). Uniform absolute total pressure and temperature were chosen for the inlet boundary conditions. At outlet, the condition "massflow imposed with pressure adaptation" is used. For turbulence closure, the two-equation SST model was chosen. The turbulence intensity is assessed based on the Reynolds number and on a turbulent length scale. Minimum and maximum values of this parameter is respectively about 3% and 4%. Steady RANS simulations were performed, using the commercial solver FINE™/Turbo developped by NUMECA International (2015).

VALIDATION OF NUMERICAL SIMULATIONS

The numerical predictivity of the code is reported for three quantities as depicted in Fig. 3 for Fan 1. At rotor exit, small differences on both absolute flow angle and absolute total pressure

are reported for Fan 1 at $\hat{\phi}^* = 0.6$ and $\hat{\phi}^* = 1$. On the contrary, greater differences arise at $\hat{\phi}^* = 2$, from $h/H = 30\%$ to blade tip for these two quantities. This discrepancy is associated with a poor prediction of the massive separation typical of turbine modes. This causes the bad prediction of the work exchange (Euler theorem). Finally, the general shape of axial velocity distributions of Fan 1 are fairly caught by numerical model for all operating points but velocity levels are not accurately estimated.

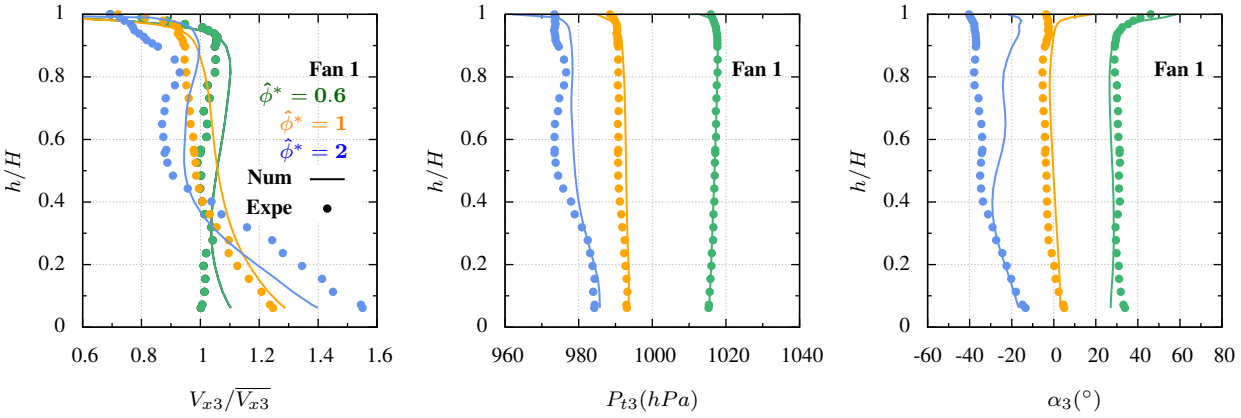

Figure 3: Experimental radial distributions of adimensionalized axial velocity, total pressure and absolute angle at rotor outlet for Fan 1.

Figure 4 shows that numerical results obtained on Fan 2 are in good agreement with experimental data except from $h/H = 80\%$ to blade tip at load-controlled windmill. Similarly, the separation zone is likely to be responsible for the bad prediction in this area.

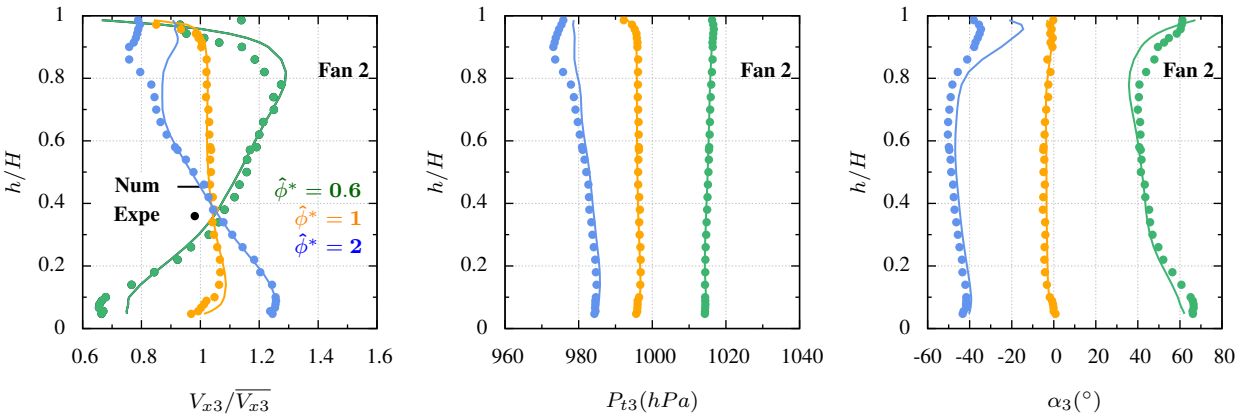

Figure 4: Experimental radial distributions of adimensionalized axial velocity, total pressure and absolute angle at rotor outlet for Fan 2.

In the following sections, numerical results are used to give qualitative understanding of flow topology through the rotor, in particular concerning tip leakage and endwalls secondary flows evolution from compressor to turbine mode.

SECONDARY FLOWS EVOLUTION FROM COMPRESSOR TO TURBINE MODES

Topology evolution

Blade to blade entropy contours are depicted in Fig. 5 from compressor to load-controlled windmill. Well known windmilling flow features such as negative incidences and massive separation can be observed. In addition, no separation is observed at $\hat{\phi}^* = 1$ despite noticeable negative incidences illustrated by streamlines

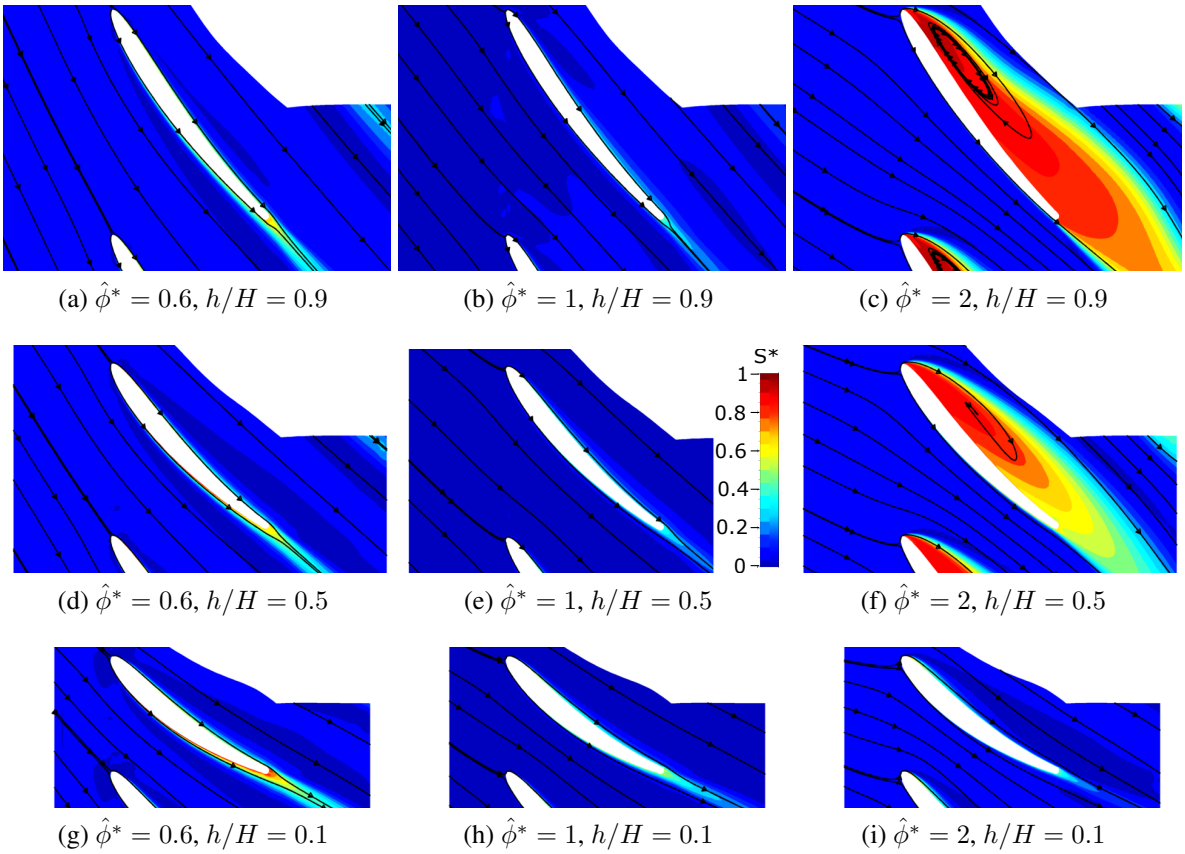

(a) $\hat{\phi}^* = 0.6, h/H = 0.9$ (b) $\hat{\phi}^* = 1, h/H = 0.9$ (c) $\hat{\phi}^* = 2, h/H = 0.9$

(d) $\hat{\phi}^* = 0.6, h/H = 0.5$ (e) $\hat{\phi}^* = 1, h/H = 0.5$ (f) $\hat{\phi}^* = 2, h/H = 0.5$

(g) $\hat{\phi}^* = 0.6, h/H = 0.1$ (h) $\hat{\phi}^* = 1, h/H = 0.1$ (i) $\hat{\phi}^* = 2, h/H = 0.1$

Figure 5: Blade to blade entropy contours

Curvature effects

Figure 6, adapted from (Lakshminarayana, 1996), introduces notations used to explain the occurrence of secondary flows in hub region. The streamlines AAA (red) and BBB (blue), represented in the absence of secondary flows, are not deflected ($R_A = R_B$). Under certain hypothesis, the momentum equations lead to Equation 2 which expresses the balance between the pressure gradient in the direction *n* and the centripetal acceleration, at point A along AAA. If the boundary layer approximation is invoked, in the near wall region, the pressure in the *b* direction is constant (no gradient normal to the side wall) so that Equation 3 is verified. As the velocity tends towards zero, the curvature radius of the streamline BBB must decrease to compensate the pressure gradient $\frac{\partial P}{\partial n}\big|_B$, so that the streamline BBB become BB'B" (green)

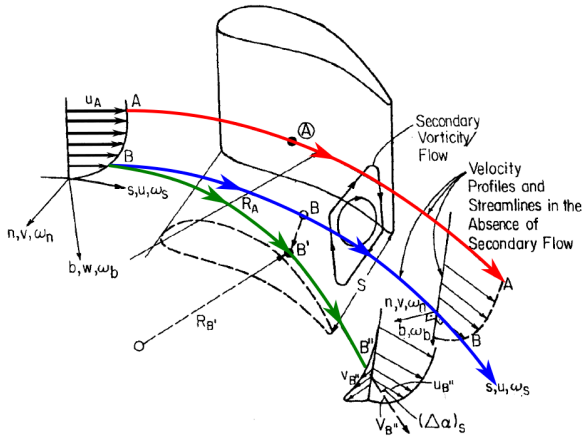

Figure 6: Secondary flow phenomenon and notation used (from (Lakshminarayana, 1996))

with $R_{B'} < R_B$.

$$\left.\frac{\partial P}{\partial n}\right|_A = \frac{\rho u_A^2}{R_A} \tag{2}$$

$$\left.\frac{\partial P}{\partial n}\right|_A = \left.\frac{\partial P}{\partial n}\right|_B \tag{3}$$

According to the previous reasoning, the streamlines curvature radius in the near wall region decreases and creates a crossflow oriented towards the low pressure zone. This phenomenon is illustrated for compressor mode, freewindmill and load-controlled windmill on Fig. 7(a), (b) and (c) respectively.

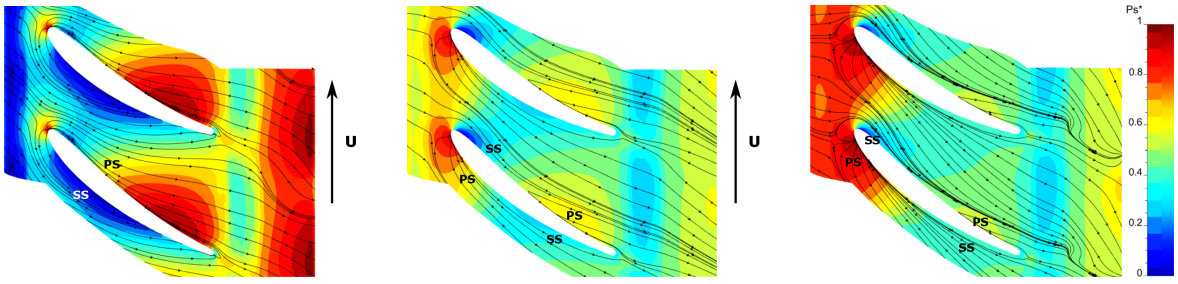

(a) $\hat{\phi}^* = 0.6$ (b) $\hat{\phi}^* = 1$ (c) $\hat{\phi}^* = 2$

Figure 7: Rotor static pressure contours and streamlines near the hub for Fan 1

In compressor mode, the streamlines are classically deviated in the direction of the rotation (upward in this figure) towards low pressure regions as illustrated in Fig. 7a. At freewindmill and load-controlled windmill, highly negative incidences cause the displacement of the stagnation point towards the trailing edge on the blade convex side. On the concave side, the lowest static pressure recorded near the leading edge is due to the great flow acceleration resulting from the leading edge bypass. The resulting pressure gradient is inverted in the first half of the blade compared to that of the compressor mode. On the second half of the blade the sign of the static pressure changes but since the bulk of pressure difference is located in the first half of the blade, an overall inversion of the lift and pressure gradient direction are observed in these operating

modes. The streamlines are thus deviated in the direction opposite to the rotation (downward in this figure). Such an continuous inversion, caused solely by the change of operating point, has not been reported so far.

As stated in (Lakshminarayana, 1996), by neglecting stream-wise pressure gradient in a turning duct, it can be proven that, $du/ds = 0$ along a mean line. Hence, the simplified form of the continuity equation gives $dw/db = -dv/dn$. Finally, the crossflow induced by curvature effects, $dv/dn \neq 0$, results in the gradient of radial velocity in the b direction, dw/db. The cross-stream distribution of radial velocity is presented on Fig. 8 (machine viewed from the front side) from compressor to turbine operations. The positive values of radial velocity observed at the hub are partly due to a meridional evolution of the vein. As can be seen, the location of positive values of radial velocities is inverted from compressor to turbine operations. It means that the sign of the streamwise vorticity changes from compressor to turbine mode. In addition, it can be underlined that the amount of negative values of the radial velocity component increase gradually from compressor to turbine operation: $Vr = 2\%V$ in compressor mode, $Vr = 9\%V$ at freewindmill and $Vr = 14\%V$ at load-controlled windmill. The interaction between these secondary flows and the massive separation is regarded in the next paragraph.

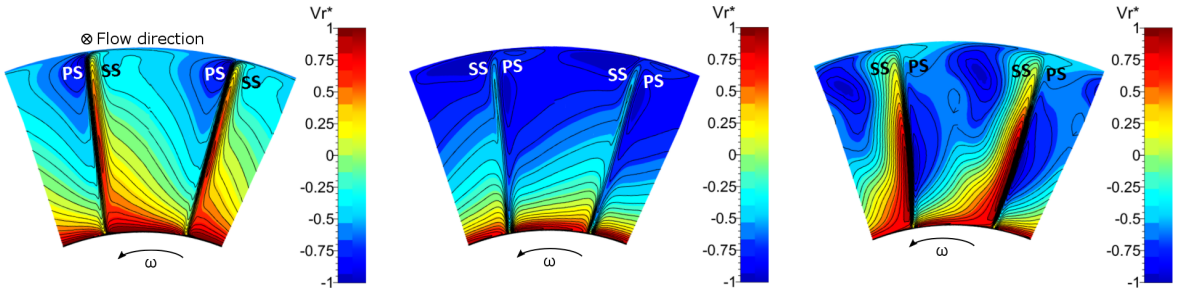

(a) $\hat{\phi}^* = 0.6$ (b) $\hat{\phi}^* = 1$ (c) $\hat{\phi}^* = 2$

Figure 8: Radial velocity at rotor outlet for Fan 1

Separation topology

Figure 9 show the separation topology for Fan 1, Fan 2 at $\hat{\phi}^* = 2$ and for a small turbofan at $\hat{\phi}^* = 1$ (Dufour et al., 2015a). For the recall, no separtation was observed for Fan 1 at $\hat{\phi}^* = 1$ (Fig. 5). The viscous stress lines, plotted on the three geometries, underline a similar reattachment line starting from the leading edge near the hub and expanding towards the trailing edge near the shroud. The linear evolution of solidity with the radius is highly suspected to be responsible for the linear pattern recorded for the reattachment line on all the machines since the radial evolution of incidence is nearly constant (Fig.10 (a)).

The 3D topology of the separated flow is presented by means of streamlines colored with the radial velocity for Fan 1 and Fan 2. Positives values of this last parameter are located in the rear part of the separated zone and in the blade skin vicinity. On the contrary, negatives values recorded near the leading edge are located at a given distance of the blade. The blade-to-blade distribution of radial velocity, given on Fig. 10(b), is very similar to that reported by (Gill, 2011). The same result is also observed for Fan 2 which suggest suggest the possible generalization of the separation topology. The latter can be explained by the static pressure gradient recorded in the passage and visible on Fig. 10(b). The highest radial pressure gradient,

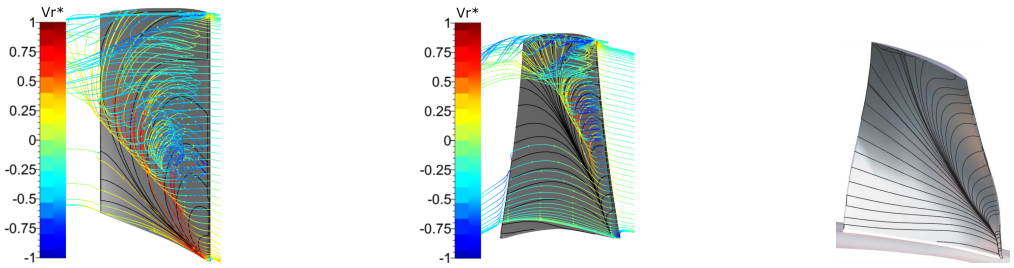

Figure 9: Stress lines and streamlines colored with radial velocities for Fan 1 (a) and Fan 2 (b) at load-controlled windmill, for a small turbofan at freewindmill (c) from (Dufour et al., 2015a)

illustrated by the highest isoline density, is located at the leading edge. It acts on the streamline curvature and results in a hubward motion of the fluid in this region, as illustrated by the zone of negative radial velocity in the blade to blade view. For the same reason, the fluid moves upward in the trailing edge region leading to a widening of the rotor wakes near the tip. Rotor/stator interactions will be modified by the ingestion of widened rotor wakes. This effect may have a significant impact on stator losses. Such effects cannot be captured by mixing plane simulations.

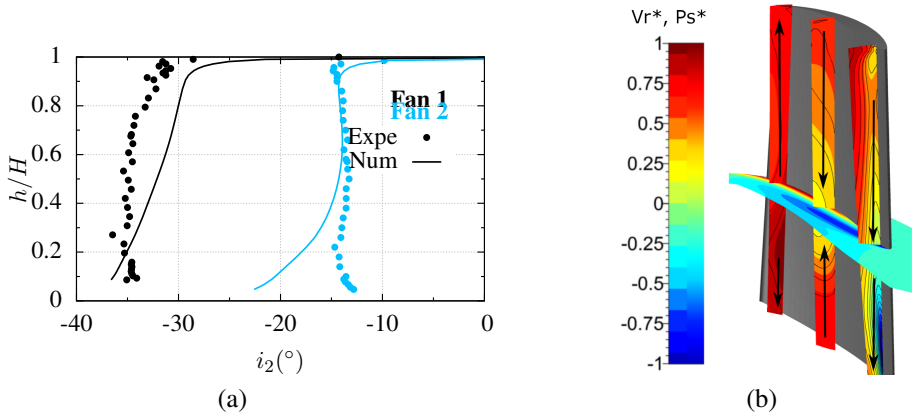

Figure 10: Experimental radial distributions of incidences (a) at $\hat{\phi}^* = 2$. Blade-to-blade contour of radial velocity and cross-stream contours of static pressure for Fan 1 at loaded windmill (b)

Tip leakage flow

This section aims at analyzing the tip leakage flow evolution from compressor to turbine modes. This secondary flow comes from the pressure differences between the two sides of the blade at the tip. This last result is presented on Fig. 11a for Fan 1 and on Fig. 11b for Fan 2 at $\hat{\phi}^* = 0.6$, at $\hat{\phi}^* = 1$ and at $\hat{\phi}^* = 2$. For the clarity of the discussion, pressure coefficient on the concave side (referred as PS) and on the convex side (referred as SS) of the blade are represented with solid and dotted lines respectively. For Fan 1, an inversion of the lift force direction is recorded between compressor and turbine modes. This implies that the tip leakage flow is located on the convex side of the blade in compressor operation and on the concave side of the blade in turbine mode. The pressure coefficient recorded in freewheeling condition

shows the existence of a neutral point, near 30% of the chord, where no lift is created. As a consequence, the tip leakage flow crosses the blade near this point.

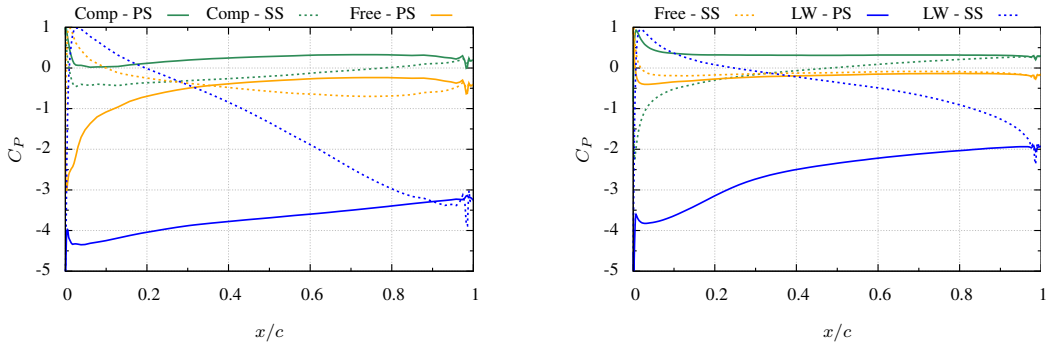

(a) Fan 1 (b) Fan 2

Figure 11: Pressure coefficient on concave (PS) and convex side (SS) of the blade in compressor mode, freewindmill and load-controlled windmill at $h/H = 90\%$

This leads to an expected evolution of the tip leakage flow, suspected to be generic for conventional fans. This topology is illustrated on Fig. 12. On the contrary, Fan 2 is characterized by a non conventional pressure coefficient distribution at $\hat{\phi}^* = 1$ where the pressure on both sides of the blade is identical, leading to an absence of tip leakage flow, as visible on Fig. 13(b).

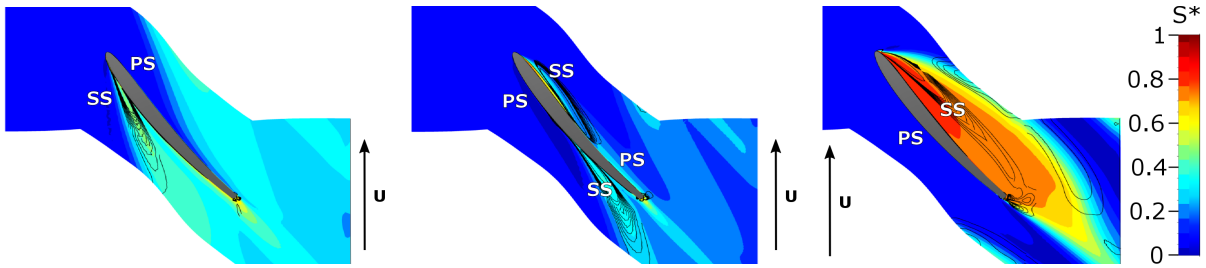

(a) $\hat{\phi}^* = 0.6$ (b) $\hat{\phi}^* = 1$ (c) $\hat{\phi}^* = 2$

Figure 12: Tip leakage flow illustration : Q-criterion isolines and normalized entropy for Fan 1

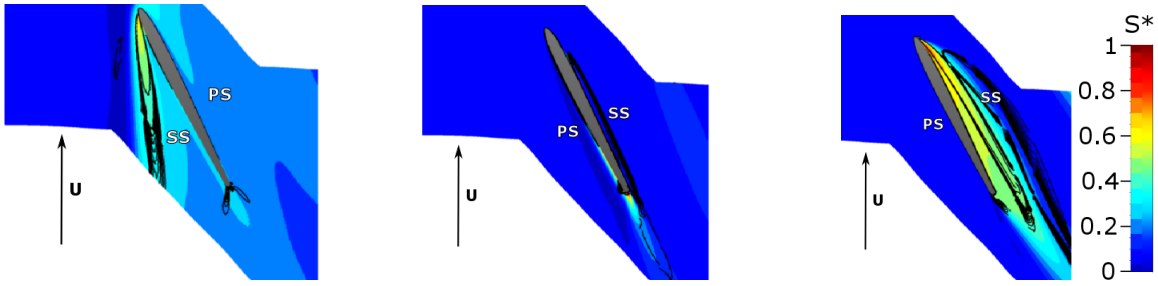

(a) $\hat{\phi}^* = 0.6$ (b) $\hat{\phi}^* = 1$ (c) $\hat{\phi}^* = 2$

Figure 13: Tip leakage flow illustration : Q-criterion isolines and normalized entropy for Fan 2

CONCLUSIONS

In this paper, generic mechanisms are proposed to explain the origin of rotor separation topology of windmilling fans. Local experimental results are presented to assess the numerical predictivity of the RANS mixing plane simulations which support the local flow topology study. The main findings of this paper can be summarized as follow:

1. In compressor mode, the curvature effects inside the hub boundary layer create crossflow in the direction of the rotation. A continuous inversion of the pressure gradient normal to the streamwise direction is observed while switching from compressor to load-controlled windmill. This evolution is responsible for the inversion of the curvature effects which generate crosstream in the direction opposite to the rotation at load-controlled windmill.

2. The induced radial velocities are consequently observed on the two different sides of the blade depending on the considered operating mode. In any case, positive radial velocities are recorded on the suction side of the blade which is inverted in the two functioning.

3. Positive radial velocities and decrease in solidity from hub to shroud are responsible for the generic triangular shape of the separation zone, the inner layer being only separated near the leading edge while the outer layer being completely separated. The recirculation inside the separation is also generic. The fluid moves hubward near the leading edge and tipward near the trailing edge. The wider wakes impacting the stator near the shroud need to be numerically captured for a better loss prediction and turbine efficiency optimization.

4. A specific evolution of the tip leakage flow topology is presented. The tip vortex is located on one side of the blade in compressor operation, passes through the blade at mid-chord in freewheeling mode and is on the other side in loaded windmilling conditions.

ACKNOWLEDGEMENTS

This study was performed within the scope of the CORAC GENOME project, which aims at optimizing power managements in more electric aircrafts. The authors are grateful to the CORAC consortium, created on the government initiative to harmonize research efforts in aeronautics. The authors would like to express their gratitude to the technical staff for their countless involvements in the experimental facility improvements.

REFERENCES

Binder, N., Courty-Audren, S.-K., Duplaa, S., Dufour, G., and Carbonneau, X. (2015). *Theoretical analysis of the aerodynamics of low-speed fans in free and load-controlled windmilling operation*. *Journal of Turbomachinery*, 137(10):101001–12.

Courty-Audren, S.-K. (2015). *Identification et compréhension des mécanismes aérodynamiques liés au potentiel de récupération d'énergie. Application à un ventilateur axial subsonique en autorotation*. PhD thesis, ISAE-SUPAERO.

Courty-Audren, S.-K., Carbonneau, X., Binder, N., and Challas, F. (2013). *Comparaison des méthodes numériques stationnaire et instationaires dans la prédiction d'écoulements décollés*. In *Proceedings of the 10th European Conference on Turbomachinery*. April 15-19, Lappeenranta, Finland. ETC2013-094.

Cumpsty, N. A. (2004). *Compressor aerodynamics*. Krieger.

Dufour, G., García Rosa, N., G., and Duplaa, S. (2015a). Validation and flow structure analysis in a turbofan stage at windmill. In *Journal of Power and Energy*.

Dufour, G., Margalida, G., and García Rosa, N. (2015b). *Integrated flow simulation of the fan and high-pressure compressor stages of a turbofan at windmill*. In *Proceedings of the 10th European Conference on Turbomachinery*. March 23-27, Madrid, Spain. ETC2015-150.

Gill, A. (2011). *Four quadrant axial flow compressor performance*. PhD thesis, Stellenbosch University.

Gunn, E. J. and Hall, C. A. (2015). Loss and deviation in windmilling fans. In *Proceedings of the 11th European Conference on Turbomachinery*. March 23-27, Madrid, Spain. ETC2015-061.

Japikse, D. and Baines, N. C. (1997). *Introduction to turbomachinery*. Concepts ETI.

Lakshminarayana, B. (1996). *Fluid Dynamics and Heat Transfer of Turbomachinery*. John Wiley & Sons.

NUMECA International (2015). *User Manual FINE^{TM}/Turbo v10.2*. Brussels, Belgium.

Ortolan, A., Carbonneau, X., Binder, N., and Challas, F. (2016). *Experimental and numerical flow analysis of low-speed fans at highly loaded windmilling conditions*. In *ASME Turbo Expo*. June 13-17, Seoul, South Korea. GT2016-56577.

Ortolan, A., Carbonneau, X., Binder, N., Challas, F., and Meauze, G. (2015). *Innovative fan design for both high compressor and windmilling performance*. In *Proceedings of the 12th International Symposium on Experimental and Computational Aerothermodynamics of Internal Flows*. July 13-16, Lerici, Italy. ISAIF12-068.

Prasad, D. and Lord, W. K. (2010). *Internal losses and flow behavior of a turbofan stage at windmill*. *Journal of Turbomachinery*, **132**(3):031007–10.

Turner, R. C. and Sparkes, D. W. (1963). *Complete characteristics for a single stage axial flow fan*. In *Proceedings of the Institution of Mechanical Engineers*, **178**(9), pages 14–27.